


A comprehensive calculation of the Primakoff process and the solar axion flux

Quan-feng Wu^{a,b} Xun-Jie Xu^a

^a*Institute of High Energy Physics, Chinese Academy of Sciences, Beijing 100049, China*

^b*University of Chinese Academy of Sciences, Beijing 100049, China*

E-mail: wuquanfeng@ihep.ac.cn, xuxj@ihep.ac.cn

ABSTRACT: The Primakoff process plays a crucial role in axion production in astrophysical environments and laboratories. Given the rising interest in axion physics and many on-going experimental activities, we conduct a comprehensive calculation of this process and carefully examine several aspects that have been neglected in the literature. In particular, our calculation is valid for axions with significantly large masses, which would be of importance to axion searches utilizing crystal and liquid xenon detectors. We present the most updated calculation of the Primakoff solar axion flux, with a simple parametrization that is applicable to a broad range of axion masses up to a few tens of keV. Our code is publicly available at GitHub .

Contents

1	Introduction	1
2	General setup	2
2.1	Lagrangian	2
2.2	Kinematics	3
3	The cross section of the Primakoff process	6
3.1	Scattering off electric charges	6
3.2	Including nuclear magnetic moments	8
3.3	Target particles of spin 0, spin 1/2, ...	10
3.4	Pseudoscalar versus scalar	11
3.5	Debye-Hückel screening	11
3.6	Coherent scattering with large-scale magnetic fields	13
3.7	Summary	15
4	Solar axion flux	16
5	Conclusions	18
A	The QFT approach to coherent scattering with background fields	18
B	Full expression of the total cross section including Debye-Hückel screening	22

1 Introduction

The Primakoff process [1], originally proposed for photoproduction of the π^0 meson in a nuclear electric field, currently plays a crucial role in the active field of searching for axions, a type of new light pseudoscalars well motivated by the strong CP problem [2–5]. In stellar environments, axions could be abundantly produced via the Primakoff process, leading to various interesting astrophysical consequences [6, 7]. In particular, solar axions might be detectable in laboratories via the inverse Primakoff process, motivating a number of experimental searches [8–12].

Given the importance of the Primakoff process in axion studies and the actively ongoing experimental searches, we believe it is timely to revisit this process and carefully examine several aspects that have been neglected in the literature. For instance, the simplest Primakoff cross section of a photon scattering off a nucleus in the vacuum, obtained by treating the electric field around the nucleus as a classical field, cannot fully take into account the recoil, spin, and magnetic moment of the nucleus. The widely-adopted formula

for the Primakoff production of axions in plasma with Debye-Hückel screening included, first derived in Ref. [13], is not applicable to massive axions if the mass is significant.¹ Although the axion mass effect is negligible in helioscope experiments like CAST which quickly loses sensitivity above a few eV [15], it could be of importance to experiments utilizing crystal [8, 10–12] or liquid xenon [16–19] detectors if the search range extends to keV or higher.

In this work, we present a comprehensive calculation of the Primakoff process, aiming at providing a revised solar neutrino flux valid in the full mass range. Such a calculation would be particularly useful for phenomenological studies on solar axions [18–32]. We start with a rigorous treatment of the kinematics and an exact evaluation of the Feynman diagram of Primakoff scattering in the vacuum [33]. Then step by step, we take into account more factors such as the magnetic moment and spin of the target particle, the difference between scalar and pseudoscalar, and Debye-Hückel screening, and discuss their impact thoroughly. We also derive the coherent photon-axion conversion rate in a magnetic field in the quantum field theory (QFT) approach, which not only helps to clarify subtleties arising from the mismatch between the incoming and outgoing momenta, but also allows us to obtain the conversion rate for non-relativistic axions. This could be important to axion dark matter conversion in e.g. neutron star magnetospheres [34–49].

This paper is organized as follows. In Sec. 2, we setup the notation used in this work and elucidate the correlations among multiple kinematic variables. In Sec. 3, we present the detailed calculation of the Primakoff process and discuss the impact of many previously neglected factors. Then in Sec. 4 we apply the calculation to the latest solar model and obtain a practically useful expression for the solar axion flux. The codes for the flux calculation is publicly accessible via GitHub². Finally we conclude in Sec. 5 and relegate some details to the appendix.

2 General setup

2.1 Lagrangian

The electromagnetic interaction of the axion is given by the following effective Lagrangian:


$$\mathcal{L} \supset -\frac{g_{a\gamma}}{4} a F_{\mu\nu} \tilde{F}^{\mu\nu}, \quad (2.1)$$

where $g_{a\gamma}$ is a dimensional coupling constant, a denotes the axion field, $F_{\mu\nu} \equiv \partial_\mu A_\nu - \partial_\nu A_\mu$ is the electromagnetic field tensor, and \tilde{F} is the Hodge dual of the field strength tensor F , i.e.,

$$\tilde{F}^{\mu\nu} = \frac{1}{2} \varepsilon^{\mu\nu\rho\sigma} F_{\rho\sigma}, \quad (2.2)$$

with the convention $\varepsilon^{0123} = -\varepsilon_{0123} = 1$.

¹An earlier study [14] considered the production of heavy (keV to sub-MeV) axions in red giants, in which the mass effect was important and taken into account, but the screening effect was not included.

² <https://github.com/Fenyutanchan/Solar-Axion-Primakoff-Flux.git>

While Eq. (2.1) can naturally arise from the Peccei-Quinn solution to the strong CP problem [2–5], it is also one of the simplest interaction terms³ that couple a new light (pseudo)scalar to the electromagnetic field. Given that the electromagnetic field is highly manipulable, Eq. (2.1) also serves as a phenomenologically interesting avenue for new physics exploration.

In addition to the pseudoscalar interaction, one may also consider a scalar coupled to the electromagnetic field:

$$\mathcal{L} \supset -\frac{g_{\phi\gamma}}{4}\phi F_{\mu\nu}F^{\mu\nu}, \quad (2.3)$$

where ϕ is a CP-even scalar with a similar coupling $g_{\phi\gamma}$. Although in this work we mainly focus on the pseudoscalar case, our results can be readily applied to the scalar case, as the difference is negligible if particle spins or polarizations are averaged out—see Secs. 3.4 and 3.6.

From Eqs. (2.1) and (2.3), it is straightforward to write down the Feynman rule of the a - A - A (or ϕ - A - A) vertex:

$$\begin{array}{c} \text{---} p \text{---} \\ \diagup \\ \text{---} k \text{---} \\ \diagdown \\ \text{---} k' \text{---} \\ \text{---} \nu \text{---} \end{array} \begin{array}{c} \mu \\ \diagdown \\ \diagup \\ \nu \end{array} = \begin{cases} ig_{a\gamma}\varepsilon^{\mu\nu\rho\sigma}k_\sigma k'_\rho & \text{(pseudoscalar)} \\ ig_{\phi\gamma}[(k \cdot k')g_{\mu\nu} - k_\nu k'_\mu] & \text{(scalar)} \end{cases}. \quad (2.4)$$

They lead to almost identical decay widths:

$$\Gamma_{a \rightarrow \gamma\gamma} = \frac{g_{a\gamma}^2 m_a^3}{64\pi}, \quad \Gamma_{\phi \rightarrow \gamma\gamma} = \frac{g_{\phi\gamma}^2 m_\phi^3}{64\pi}. \quad (2.5)$$

In terms of electric and magnetic fields, $(\mathbf{E}, \mathbf{B}) \equiv (-\nabla A^0 - \partial_t \mathbf{A}, \nabla \times \mathbf{A})$, the interactions in Eqs. (2.1) and (2.3) can be written as

$$-\frac{1}{4}aF_{\mu\nu}\tilde{F}^{\mu\nu} = (\mathbf{E} \cdot \mathbf{B})a, \quad (2.6)$$

$$-\frac{1}{4}\phi F_{\mu\nu}F^{\mu\nu} = \frac{1}{2}(|\mathbf{E}|^2 - |\mathbf{B}|^2)\phi, \quad (2.7)$$

which will be used in the calculation of photon-axion conversion in macroscopic magnetic fields.

2.2 Kinematics

We consider the Primakoff process, $\gamma + X \rightarrow a + X$, where the target particle X can be an electron, a proton, or a heavier nucleus. The masses of X and a are denoted by m_X and m_a , respectively. For $m_a = 0$, it is elastic scattering with relatively simple kinematics.

³At dimension-three level, one could write down the operator $\phi A^\mu A_\mu$ where ϕ is a generic scalar. But this operator does not respect the gauge symmetry of QED. At dimension-four level, operators like $\phi^* A^\mu \partial_\mu \phi$ could appear but ϕ has to be a charged scalar which, with a mass below typical collider energy scales and a quantized charge, would be efficiently produced on colliders via the Drell-Yang process and thus be ruled out. Hence we conclude that the simplest operators of light scalars interacting with the electromagnetic field should be at least dimension-five.

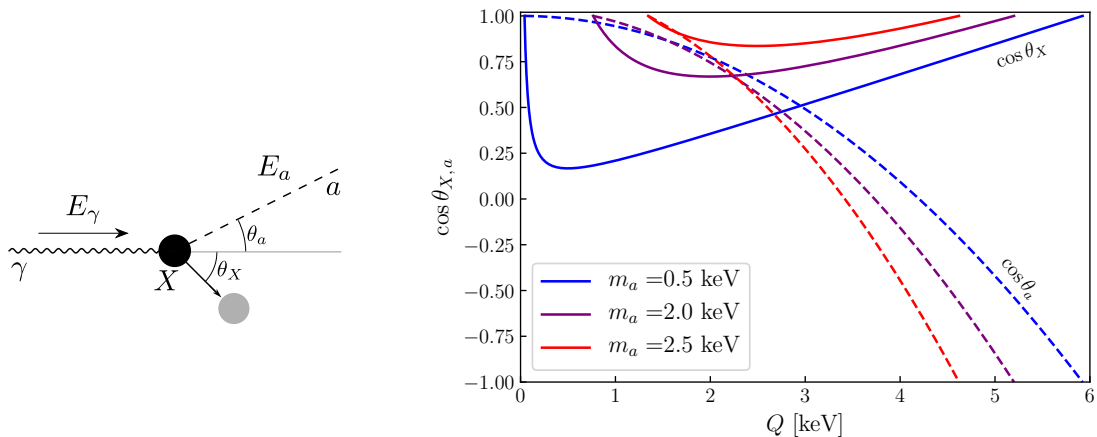


Figure 1. The kinematics of the Primakoff process. Left panel: a schematic representation of kinematic variables θ_a and θ_X . Right panel: The variation of $\cos\theta_a$ (dashed lines) and $\cos\theta_X$ (solid lines) as functions of the momentum transfer Q , assuming $E_\gamma = 3$ keV, $m_a \in \{0.5, 2.0, 2.5\}$ keV, and $m_X = 0.511$ MeV.

For $m_a \neq 0$ (e.g., m_a being comparable to the incoming photon energy), the kinematics becomes more complicated, as we shall elaborate below.

We denote the incoming photon energy and the outgoing axion energy by E_γ and E_a , respectively. The angle between the outgoing axion and the incoming photon is θ_a . For the X particle after scattering, we define a similar angle θ_X and denote its kinetic energy by T_X . These kinematic variables are illustrated by the left panel of Fig. 1.

We further denote the four momenta of the incoming photon, the outgoing axion, the X particle before and after scattering by p_1^μ , p_3^μ , p_2^μ and p_4^μ , respectively. Without loss of generality, we assume the following explicit forms for these momenta:

$$p_1^\mu = (E_\gamma, -E_\gamma, 0, 0), \quad (2.8)$$

$$p_2^\mu = (m_X, 0, 0, 0), \quad (2.9)$$

$$p_3^\mu = (E_a, \mathbf{p}_3), \quad (2.10)$$

$$p_4^\mu = (m_X + T_X, \mathbf{p}_4). \quad (2.11)$$

The momentum transferred from the photon to the X particle, $q^\mu \equiv p_1^\mu - p_3^\mu = p_4^\mu - p_2^\mu$, is spacelike, $q^2 = q \cdot q < 0$. Hence we define

$$Q \equiv \sqrt{-q^2}, \quad (2.12)$$

which quantifies the momentum transfer.

Next, we employ the Mandelstam variables: $s \equiv (p_1 + p_2)^2$, $t \equiv (p_1 - p_3)^2$, and $u \equiv (p_1 - p_4)^2$. The s variable can be computed directly from Eqs. (2.8) and (2.9). The t variable can be computed from $t = (p_2 - p_4)^2 = p_2^2 - 2p_2 \cdot p_4 + p_4^2$ with $p_{2,4}^2 = m_X^2$ and $p_2 \cdot p_4 = m_X(m_X + T_X)$. The u variable can be obtained by $\Sigma_{m^2} - s - t$ where Σ_{m^2} denotes the sum of squares of all masses in the initial and final states. In terms of T_X , the

Mandelstam variables are given by

$$s = m_X(2E_\gamma + m_X), \quad (2.13)$$

$$t = -2m_X T_X, \quad (2.14)$$

$$u = m_X^2 - 2E_\gamma m_X + 2m_X T_X + m_a^2. \quad (2.15)$$

The angles θ_a and θ_X can be obtained by computing $p_1 \cdot p_3$ and $p_1 \cdot p_4$ using Eqs. (2.10) and (2.11), and then comparing them with $p_1 \cdot p_3 = \frac{1}{2}(p_1^2 + p_3^2 - t)$ and $p_1 \cdot p_4 = \frac{1}{2}(p_1^2 + p_4^2 - u)$:

$$\cos \theta_X = \frac{2T_X(E_\gamma + m_X) + m_a^2}{2E_\gamma \sqrt{2m_X T_X + T_X^2}}, \quad (2.16)$$

$$\cos \theta_a = \frac{2E_\gamma^2 - 2E_\gamma T_X - 2m_X T_X - m_a^2}{2E_\gamma \sqrt{E_\gamma^2 - 2E_\gamma T_X + T_X^2 - m_a^2}}. \quad (2.17)$$

For later use, we also present an analytical expression of $d \cos \theta_a / dT_X$:

$$\frac{d \cos \theta_a}{dT_X} = \frac{-2E_\gamma^2 m_X + E_\gamma(2m_X T_X + m_a^2) + m_a^2(2m_X + T_X)}{2E_\gamma(E_\gamma^2 - 2E_\gamma T_X - m_a^2 + T_X^2)^{3/2}}. \quad (2.18)$$

The kinetic energy T_X cannot vary arbitrarily, otherwise $\cos \theta_X$ and $\cos \theta_a$ in Eqs. (2.16) and (2.17) could exceed the allowed interval $[-1, 1]$. The kinematically allowed range of T_X is given by

$$T_{\min} \leq T_X \leq T_{\max}, \quad (2.19)$$

with

$$T_{\min} = \frac{2E_\gamma^2 m_X - m_a^2(E_\gamma + m_X) - E_\gamma \sqrt{4E_\gamma^2 m_X^2 - 4m_a^2 m_X(E_\gamma + m_X) + m_a^4}}{2m_X(2E_\gamma + m_X)}, \quad (2.20)$$

$$T_{\max} = \frac{2E_\gamma^2 m_X - m_a^2(E_\gamma + m_X) + E_\gamma \sqrt{4E_\gamma^2 m_X^2 - 4m_a^2 m_X(E_\gamma + m_X) + m_a^4}}{2m_X(2E_\gamma + m_X)}. \quad (2.21)$$

In the limit of $m_a \rightarrow 0$, Eq. (2.20) vanishes, as is expected from elastic scattering. For small m_a , we obtain the following expansion in m_a :

$$T_{\min} \approx \frac{m_a^4}{8E_\gamma^2 m_X} + \mathcal{O}(m_a^6), \quad (2.22)$$

$$T_{\max} \approx \frac{2E_\gamma^2}{2E_\gamma + m_X} \left(1 - \frac{E_\gamma + m_X}{2E_\gamma^2 m_X} m_a^2 \right) + \mathcal{O}(m_a^4). \quad (2.23)$$

In the right panel of Fig. 1, we vary T_X from its minimum to its maximum (the corresponding value of Q is given by $Q = \sqrt{2m_X T_X}$) and plot the variation of $\cos \theta_X$ and $\cos \theta_a$ according to Eqs. (2.16) and (2.17). As the figure shows, when Q increases from the kinematically allowed minimum to the maximum, $\cos \theta_a$ decreases monotonically from 1 to -1 , while $\cos \theta_X$ first decreases and then increases, with a minimum appearing in the middle.

The allowed interval of T_X (or Q) shrinks as m_a increases. From Eqs. (2.16) and (2.17) we obtain that the interval vanishes (i.e., $T_{\min} = T_{\max}$) when m_a reaches

$$m_a^{\max} = \sqrt{2E_\gamma m_X + m_X^2} - m_X \approx E_\gamma - \frac{E_\gamma^2}{2m_X} + \mathcal{O}\left(\frac{E_\gamma^3}{m_X^3}\right). \quad (2.24)$$

Eq. (2.24) implies that the maximal axion mass allowed by the kinematics is slightly below the photon energy E_γ , assuming $E_\gamma/m_X \ll 1$.

3 The cross section of the Primakoff process

In this section, we present our calculations of the Primakoff process at multiple levels starting from the simplest scenario where only the electric charge form factor of the target particle is considered, with more factors to be taken into account in subsequent subsections. Whenever possible, we compare our results with known results in the literature.

3.1 Scattering off electric charges

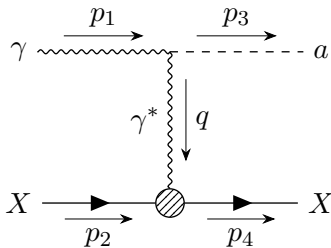


Figure 2. Primakoff production of the axion.

We first consider that X is an electrically charged fermion interacting with the photon via

$$\mathcal{L} \supset e \bar{\psi}_X F_1(q^2) \gamma^\mu A_\mu \psi_X, \quad (3.1)$$

where ψ_X denotes the Dirac spinor of X and $F_1(q^2)$ is the charge form factor of X . The Feynman diagram of $\gamma + X \rightarrow a + X$ is presented in Fig. 2. Given the photon-axion vertex in Eq. (2.4), the squared matrix element of this process reads:

$$|\mathcal{M}|^2 = \frac{1}{2} \cdot \frac{1}{2} \cdot \left| g_{a\gamma} \epsilon_\mu \epsilon^{\mu\nu\alpha\beta} p_{1\alpha} q_\beta \frac{1}{q^2} e F_1 \bar{u}_4 \gamma_\nu u_2 \right|^2, \quad (3.2)$$

where ϵ , u_4 and u_2 denote the initial photon, final and initial fermion states, respectively. The two $1/2$ factors account for spin and polarization average.

Given the squared matrix element, the differential cross section is computed by [50]

$$\frac{d\sigma}{dt} = \frac{|\mathcal{M}|^2}{64\pi s |\mathbf{p}_{1\text{cm}}|^2}, \quad (3.3)$$

where $s|\mathbf{p}_{1\text{cm}}|^2 = (p_1 \cdot p_2)^2 - p_1^2 p_2^2 = (s - m_X^2)^2/4$.

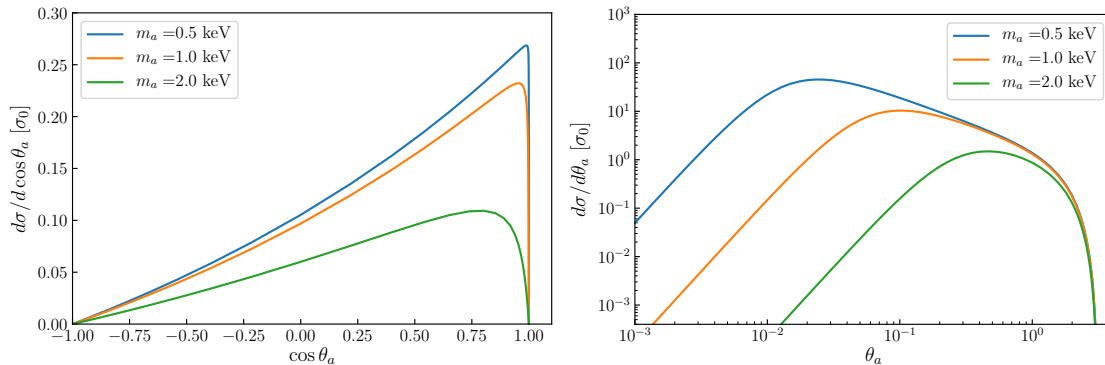


Figure 3. The differential cross sections $d\sigma/d\cos\theta_a$ (left panel) and $d\sigma/d\theta_a$ (right panel) for $m_a \in \{0.5, 1, 2\}$ keV, $E_\gamma = 3$ keV, and $m_X = m_e$. The unit σ_0 is defined in Eq. (3.7).

By applying the standard trace technology and contracting all Lorentz indices, we obtain the explicit form of $|\mathcal{M}|^2$ expressed in terms of the Mandelstam variables, among which u can be replaced by $\Sigma_{m^2} - s - t$ and s by $m_X(2E_\gamma + m_X)$ according to Eq. (2.13). Then substituting the result of $|\mathcal{M}|^2$ into Eq. (3.3), we obtain

$$\frac{d\sigma}{dt} = \frac{\alpha g_{a\gamma}^2 F_1^2}{16} \left[-\frac{(t - m_a^2)^2 + 4E_\gamma^2 t}{2E_\gamma^2 t^2} + \frac{m_a^2 - t}{E_\gamma t m_X} - \frac{(t - m_a^2)^2}{4E_\gamma^2 t m_X^2} \right], \quad (3.4)$$

where the three terms in square brackets are proportional to $(1/m_X)^n$ with $n = 0, 1,$ and 2 . Consequently, the typical magnitudes of these terms are in descending order from the left to the right. However, in certain limits, the second term can be as large as the first, resulting a cancellation between them, as we will see later. We have checked that Eq. (3.4) agrees with Eq. (3) in Ref. [33] if the last term $\propto (1/m_X)^2$ is omitted and the F_1 form factor is adjusted to the definition in Ref. [33]. In Sec. 3.3 we show that the $(1/m_X)^2$ term should be absent for spin-0 target particles.

Eq. (3.4) can be further written in terms of T_X :

$$\frac{d\sigma}{dT_X} = \frac{\alpha g_{a\gamma}^2 F_1^2}{8E_\gamma} \cdot \frac{T'_X}{T_X} \cdot J, \quad J \equiv \frac{2E_\gamma^2 T_X - m_X T_X'^2}{2E_\gamma T_X T_X'} - 1 + \frac{T'_X}{2E_\gamma}, \quad (3.5)$$

where $T'_X = T_X + m_a^2/(2m_X)$. The differential cross sections can also be written into the form of $d\sigma/d\cos\theta_a$ or $d\sigma/d\theta_a$, by multiplying proper Jacobian $dT_X/d\cos\theta_a$ or $dT_X/d\theta_a$ —see Eq. (2.18) for the analytical expression. In Fig. 3, we select a few representative values of m_a and present $d\sigma/d\cos\theta_a$ and $d\sigma/d\theta_a$ as functions of $\cos\theta_a$ and θ_a respectively.

From Eq. (3.4), we obtain the total cross section:

$$\sigma_{\text{tot}} \equiv \int \frac{d\sigma}{dT_X} dT_X \approx \sigma_0 Q_X^2 (L - 1 + K^2) + \mathcal{O}(m_a^2), \quad (3.6)$$

where we have taken $F_1^2(q^2) \rightarrow Q_X^2$ with Q_X the electric charge of X , and (σ_0, L, K) are defined as

$$\sigma_0 \equiv \frac{1}{8} \alpha g_{a\gamma}^2, \quad (3.7)$$

$$K \equiv \frac{E_\gamma}{2E_\gamma + m_X}, \quad (3.8)$$

$$L \equiv \log \left[\frac{16E_\gamma^3 m_X K}{m_a^4} \right]. \quad (3.9)$$

The above result is obtained by expanding most quantities in m_a except for a logarithmic part which is kept as the L term. In the limit of $m_a \rightarrow 0$, the total cross section diverges, which is a well-known feature of the Primakoff scattering in the vacuum [13]. In an electrically neutral medium, the divergence can be canceled out after taking the Debye-Hückel screening into account—see Sec. 3.5.

Within a rather broad range of m_a , σ_0 reflects the typical magnitude of σ_{tot} , since $L - 1 + K^2$ can be roughly viewed as an $\mathcal{O}(1 \sim 10)$ quantity. In particular, it implies that the total cross section is nearly independent of the target mass, insofar as $E_\gamma \ll m_X$. Indeed, by taking $K \approx E_\gamma/m_X \ll 1$, we obtain $L \approx \log(16E_\gamma^4/m_a^4)$ and

$$\sigma_{\text{tot}}(\gamma + e^- \rightarrow a + e^-) - \sigma_{\text{tot}}(\gamma + p \rightarrow a + p) \approx \sigma_0 \mathcal{O}\left(\frac{E_\gamma}{m_e}\right). \quad (3.10)$$

Therefore, the Primakoff cross sections with the electron and the proton as target particles are almost identical, despite that their masses are very different.⁴ The fundamental reason for this is that the photon-to-axion conversion rate mainly depends on the Coulomb potential around the target particle.

There are two interesting limits of Eq. (3.4), namely the forward and backward scattering limits, corresponding to $\theta_a \rightarrow 0$ (or $T_X \rightarrow T_{\text{min}}$) and $\theta_a \rightarrow \pi$ (or $T_X \rightarrow T_{\text{max}}$). In these limits, the $(1/m_X)^n$ terms with $n = 0$ and 1 in Eq. (3.4) cancel out, for arbitrary non-vanishing m_a . This can be seen by directly substituting $t = -2m_X T_{\text{min/max}}$, with $T_{\text{min/max}}$ given by Eqs. (2.20) and (2.21), into Eq. (3.4). Conversely, one can solve the equation that equates the two terms, obtaining solutions that are exactly $T_{\text{min/max}}$ given by Eqs. (2.20) and (2.21).

Since the first two terms cancel out in the forward and backward scattering limits, we have

$$\lim_{\theta_a \rightarrow 0, \pi} \frac{d\sigma}{dt} = \frac{\sigma_0 Q_X^2}{2} \cdot \frac{(t - m_a^2)^2}{4E_\gamma^2 |t| m_X^2}, \quad (3.11)$$

or

$$\lim_{\theta_a \rightarrow 0, \pi} \frac{d\sigma}{dT_X} = \frac{\sigma_0 T_X'^2}{2E_\gamma^2 T_X} \approx \frac{\sigma_0 Q_X^2}{m_X} \times \begin{cases} 1 - \frac{m_a^2}{2E_\gamma m_X} + \mathcal{O}(m_a^4) & (\theta_a \rightarrow 0) \\ \frac{2E_\gamma m_X + m_a^2}{2E_\gamma m_X + 4E_\gamma^2} + \mathcal{O}(m_a^4) & (\theta_a \rightarrow \pi) \end{cases}. \quad (3.12)$$

In the approximation of $(m_a, E_\gamma)/m_X \ll 1$, the limit is simply given by $\sigma_0 Q_X^2/m_X$.

3.2 Including nuclear magnetic moments

The effective interaction of the proton with the photon can not be fully described by Eq. (3.1). In fact, the proton has a significantly large magnetic moment, which together

⁴For comparison, the Thomson scattering cross section $8\pi\alpha^2/(3m_X^2)$ is proportional to the inverse square of the target mass.

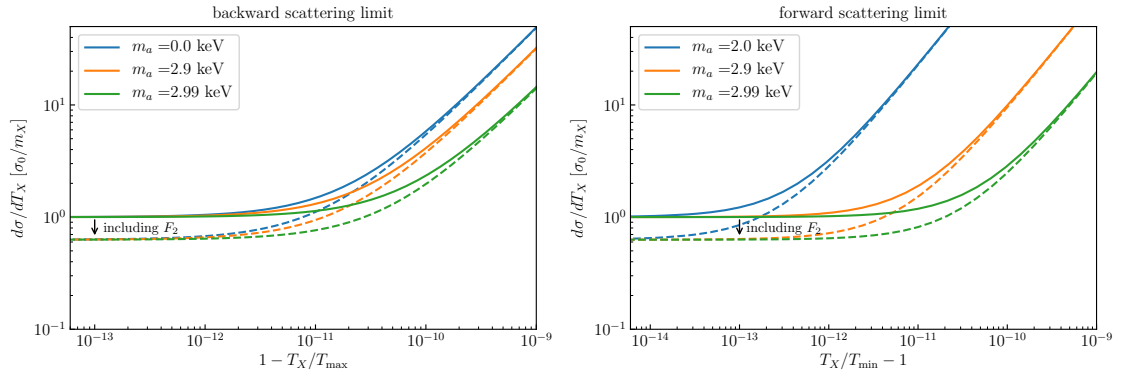


Figure 4. The effect of the proton magnetic moment on the Primakoff cross section. The solid lines represent the cross section including only the F_1 form factor—see Eq. (3.5). The dashed lines represent the cross section including both F_1 and F_2 form factors—see Eqs. (3.16) and (3.17). Note that this effect is significant only in the limit of $T_X \rightarrow T_{\max}$ (left panel) or $T_X \rightarrow T_{\min}$ (right panel). In this figure, we assume $E_\gamma = 3$ keV, $F_2 = 1.793$, and $m_X = 931$ MeV.

with the large magnetic moment of the neutron reveals that they are not fundamental fermions and should possess internal structures.

To include the magnetic moment of the target particle into our calculation, we extend Eq. (3.1) to

$$\mathcal{L} \supset \overline{e\psi_X} \left[F_1(q^2)\gamma^\mu + F_2(q^2)\frac{i\sigma^{\mu\nu}q_\nu}{2m_X} \right] A_\mu\psi_X, \quad (3.13)$$

which contains the most general form factors responsible for electromagnetic interactions of a spin-1/2 particle, assuming the conservation of P and CP symmetry.

For the proton and the neutron, the form factors in the $q^2 \rightarrow 0$ limit are

$$\text{proton: } F_1 = 1, F_2 = \mu_p - 1, \text{ with } \mu_p \approx 2.7928, \quad (3.14)$$

$$\text{neutron: } F_1 = 0, F_2 = \mu_n, \text{ with } \mu_n \approx -1.9130, \quad (3.15)$$

where μ_p and μ_n are proton and neutron magnetic moments in units of nucleon magneton [$e/(2m_p) \approx 0.1052 e \cdot \text{fm}$]. Heavy nuclei may also possess significantly large magnetic moments, which can be readily included in our calculation. For the electron, one-loop radiative corrections give rise to $F_2 \approx \alpha/(2\pi)$.

Using the effective electromagnetic vertex in Eq. (3.13), we find that the contribution of F_2 to the differential cross section can be accounted for by

$$\frac{d\sigma}{dT_X} \rightarrow (1 + \delta_T) \frac{d\sigma}{dT_X}, \quad (3.16)$$

where

$$\delta_T \equiv \frac{T_X}{2JT'_X} \left[\frac{F_2^2}{F_1^2} \left(\frac{T_X'^2}{2E_\gamma T_X} + \frac{E_\gamma - T'_X}{m_X} \right) - \frac{F_2}{F_1} \frac{2T_X'^2}{E_\gamma T_X} \right], \quad (3.17)$$

with the J factor defined in Eq. (3.5). Here the last term $\propto F_2/F_1$ comes from the interference between F_1 and F_2 . For electrically neutral (i.e. $F_1 \rightarrow 0$) particles such as the

neutron, Eqs. (3.16) and (3.17) can still be applied, with the notice that $\delta_T F_1^2$ is finite in the $F_1 \rightarrow 0$ limit and the interference vanishes.

The δ_T factor is only significant in the forward or backward scattering limit. By taking $T_X \rightarrow T_{\min}$ or T_{\max} (corresponding to $\theta_a \rightarrow 0$ or π) given by Eqs. (2.20) and (2.21), we obtain the following limit

$$\lim_{\theta_a \rightarrow 0, \pi} \delta_T = \frac{F_2}{F_1} \left(\frac{F_2}{F_1} - 2 \right), \quad (3.18)$$

which for the proton approximately equals to -0.371 .

In Fig. 4, we plot the cross sections with (dashed lines) and without (solid lines) including the F_2 factor. As is expected, the F_2 factor reduces the Primakoff cross section in the forward or backward scattering limit by about 37%.

3.3 Target particles of spin 0, spin 1/2, ...

In some circumstances, the target particle X is not a spin-1/2 fermion and may possess lower or higher spins. For example, the ${}^4\text{He}$ nucleus is a spin-0 boson while the ${}^2\text{H}$ nucleus is a spin-1 boson. Heavier nuclei may possess higher spins. In general, the effect of spin is small in low-energy scattering, roughly of the order of $T'_X/E_\gamma \sim E_\gamma/m_X$. Therefore, we only inspect the difference between spin-0 and spin-1/2 target particles quantitatively.

For a spin-0 particle, the electromagnetic vertex is formulated as

$$\mathcal{L} \supset ieF_1(q^2)A_\mu X^* \partial^\mu X + \text{h.c.}, \quad (3.19)$$

where X is a complex scalar. Eq. (3.19) can be derived from the theory of scalar QED, which would also give rise to another interaction $A_\mu A_\nu \partial^\mu X^* \partial^\nu X$, as requested by the gauge invariance. This interaction is not relevant to our analysis but could be of importance to other axion production processes.

With the interaction in Eq. (3.19), Eq. (3.2) should be modified by replacing $eF_1 \bar{u}_4 \gamma_\nu u_2 \rightarrow eF_1 (p_2 + p_4)_\nu$ and $\frac{1}{2} \cdot \frac{1}{2} \rightarrow \frac{1}{2}$ due to the absence of spin average for the initial X particle. By repeating the calculation for the spin-0 case, we find that the difference is

$$\left. \frac{d\sigma}{dT_X} \right|_{\text{spin } 1/2} - \left. \frac{d\sigma}{dT_X} \right|_{\text{spin } 0} = \frac{\alpha g_{a\gamma}^2 F_1^2 T_X'^2}{16 E_\gamma^2 T_X}, \quad (3.20)$$

which implies that the last term in the J factor of Eq. (3.5) exactly corresponds to the difference between spin-0 and 1/2.

Note that this difference is suppressed by the heavy mass of the target, since typically we have $T'_X \sim T_X \sim E_\gamma^2/m_X$ and hence $T'_X/E_\gamma \sim E_\gamma/m_X$. More generally, all spin effects should be negligible in the heavy mass limit. In particular, both the spin-0 and spin-1/2 cross sections in this limit can be written as

$$\lim_{m_X \rightarrow \infty} \frac{d\sigma}{d \cos \theta_a} = \frac{1}{4} \alpha g_{a\gamma}^2 F_1^2 \frac{|\mathbf{p}_1 \times \mathbf{p}_3|^2}{|\mathbf{q}|^4} \cdot \sqrt{1 - \frac{m_a^2}{E_\gamma^2}}, \quad (3.21)$$

which reproduces Eq. (17) in Ref. [13], except for an additional factor $\sqrt{1 - m_a^2/E_\gamma^2}$ which can be omitted when $m_a \ll E_\gamma$.

3.4 Pseudoscalar versus scalar

So far our calculation has been focused on the axion which is a pseudoscalar. For a scalar coupled to the photon via Eq. (2.3) [see also Eq. (2.7)], the resulting scattering amplitude is apparently quite different. Interestingly, after squaring the amplitude and averaging spins and polarization, the final result is exactly identical to the pseudoscalar case (here and in subsequent discussions on the pseudoscalar-scalar difference, we assume $g_{a\gamma} = g_{\phi\gamma}$). This can be verified by straightforwardly repeating the previous calculations for the scalar case with the Feynman rule in Eq. (2.4).

More generally, one can prove that this is also true for the arbitrary diagrams containing a (pseudo)scalar-photon-photon vertex with one of the photons on-shell, insofar as only the spin-averaged squared amplitude is concerned. For example, the decay widths of $\phi \rightarrow 2\gamma$ and $a \rightarrow 2\gamma$ are identical.

For the Primakoff process, we can decompose the amplitude as

$$\mathcal{M} = \epsilon_\mu \mathcal{T}^{\mu\nu} \mathcal{X}_\nu, \quad (3.22)$$

where \mathcal{X}_ν denotes the part of the amplitude that depends on the properties of the X particle, while $\epsilon_\mu \mathcal{T}^{\mu\nu}$ represents the remaining part, including the photon polarization vector ϵ_μ . For the pseudoscalar and scalar cases, the $\mathcal{T}^{\mu\nu}$ part reads:

$$\mathcal{T}_{\text{pseudo}}^{\mu\nu} = g_{a\gamma} \varepsilon^{\mu\nu\alpha\beta} p_{1\alpha} q_\beta \frac{1}{q^2}, \quad (3.23)$$

$$\mathcal{T}_{\text{scalar}}^{\mu\nu} = g_{\phi\gamma} (p_1^\nu q^\mu - g^{\mu\nu} p_1 \cdot q) \frac{1}{q^2}. \quad (3.24)$$

When squaring the amplitude, we encounter the evaluation of $\mathcal{X}_\nu \mathcal{X}_\rho^*$, which after averaging the spin (if exists) can always be written as

$$\mathcal{X}_\nu \mathcal{X}_\rho^* \xrightarrow{\text{spin average}} A p_{2\rho} p_{4\nu} + B p_{2\nu} p_{4\rho} + C m_X^2 g_{\rho\nu} + D \varepsilon^{\nu\rho\alpha\beta} p_{2\alpha} p_{4\beta}, \quad (3.25)$$

where A , B , C , and D represent quantities without Lorentz structures. Eq. (3.25) is the most general Lorentz-invariant form one can write down for $\mathcal{X}_\nu \mathcal{X}_\rho^*$.

Combing Eqs. (3.25), (3.23), (3.24), and (3.22), we obtain

$$|\mathcal{M}_{\text{pseudo}}|^2 - |\mathcal{M}_{\text{scalar}}|^2 = m_\gamma^2 g_{a\gamma}^2 \frac{4m_X^2 (A + B + 3C) - t(A + B)}{8t}, \quad (3.26)$$

where we have assumed a mass, $m_\gamma \equiv \sqrt{p_1^\mu p_{1\mu}}$, for the incoming photon. Eq. (3.26) implies that the difference could be nonzero only when the incoming photon has a different dispersion relation from the one in the vacuum. In plasma, the plasmon mass could play the role of m_γ here but since it is typically well below the photon energy, the resulting difference is small.

3.5 Debye-Hückel screening

In a medium, the Primakoff process may have a significantly altered cross section. The most prominent medium effect is the so-called Debye-Hückel screening [6, 13]. Since each

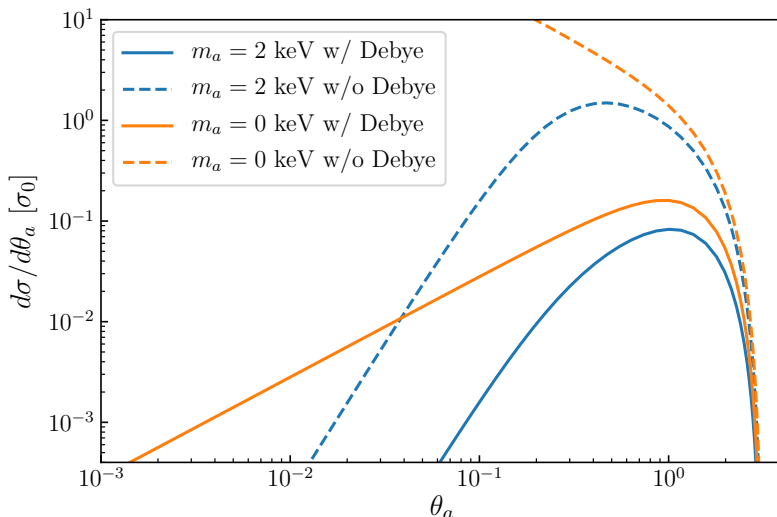


Figure 5. Primakoff cross sections with (solid) and without (dashed) Debye-Hückel screening.

electric charge in a neutral medium is in average surrounded by a charge cloud of the opposite sign, which at a sufficiently large scale is capable to cancel the Coulomb potential generated by the central charge, the effective Coulomb potential contributing to Primakoff scattering should have a finite extent, beyond which its contribution becomes negligible. Consequently, Primakoff scattering at low-momentum transfer should take a reduced charge form factor.

According to Ref. [13], Debye-Hückel screening for the Primakoff process in a thermal plasma reduces the F_1 form factor by

$$F_1^2(q^2) \rightarrow F_1^2(q^2) \frac{|q^2|}{|q^2| + \kappa_s^2}, \quad (3.27)$$

with

$$\kappa_s^2 \equiv \frac{4\pi\alpha}{T} \left(\sum_X Q_X^2 n_X \right). \quad (3.28)$$

Here T is the temperature of the plasma, and n_X denotes the number density of X . For the summation in Eq. (3.28), one should take into account all electrically charged particles in the medium, including electrons, protons and heavier nuclei, such that $\sum_X Q_X n_X = 0$. For the solar medium, κ_s is about 9 keV in the solar center and decreases in outer regions, while $(\kappa_s/T)^2 \approx 12$ is approximately constant [51].

Fig. 5 shows the impact of Debye-Hückel screening on the Primakoff cross section, assuming $E_\gamma = 3$ keV, $\kappa_s = 8$ keV, $m_a \in \{0, 2\}$ keV, and the electron as the target particle. For $m_a = 0$, $d\sigma/d\theta_a$ in the vacuum diverges in the $\theta_a \rightarrow 0$ limit, while in a medium the divergence is canceled by Debye-Hückel screening.

Including the screening effect, the total cross section is finite — for the full expression, see Appendix B. In particular, in the large m_X limit, we obtain the following analytical

expression for the total cross section:

$$\lim_{m_X \rightarrow \infty} \sigma_{\text{tot}} = \frac{\alpha g_{a\gamma}^2 Q_X^2}{8} \left[\frac{4E_\gamma^2 + \kappa_s^2 - 2m_a^2}{4E_\gamma^2} \log \frac{\kappa_s^2 + q_+^2}{\kappa_s^2 + q_-^2} + \frac{m_a^4}{4E_\gamma^2 \kappa_s^2} \log \frac{m_a^4 + \kappa_s^2 q_-^2}{m_a^4 + \kappa_s^2 q_+^2} - \xi \right], \quad (3.29)$$

where

$$\xi \equiv \sqrt{1 - \frac{m_a^2}{E_\gamma^2}}, \quad q_\pm^2 \equiv 2E_\gamma^2 (1 \pm \xi) - m_a^2. \quad (3.30)$$

In the $m_a \rightarrow 0$, Eq. (3.29) reduces to

$$\lim_{m_a \rightarrow 0} \lim_{m_X \rightarrow \infty} \sigma_{\text{tot}} = \frac{\alpha g_{a\gamma}^2 Q_X^2}{8} \left[\left(1 + \frac{\kappa_s^2}{4E_\gamma^2} \right) \log \left(1 + \frac{4E_\gamma^2}{\kappa_s^2} \right) - 1 \right], \quad (3.31)$$

which agrees with Eq. (29) in Ref. [13].

3.6 Coherent scattering with large-scale magnetic fields

In Secs. 3.1 and 3.2, we have computed the Primakoff scattering with the electric and magnetic fields of a single target particle. Electric and magnetic fields at macroscopic scales can be formed from a large collection of particles participating electromagnetic interactions, both in nature and in laboratories. In the presence of a large-scale electromagnetic field, the incoming photon can scatter coherently with the field such that the photon-axion conversion rate may exhibit the oscillation phenomenon.

Since the persistence of large-scale electric fields is rare in nature and the maintenance of strong electric fields in laboratories is more energy-consuming, here we only consider large-scale magnetic fields. Theoretically, due to electric–magnetic duality, the calculation for magnetic fields can be easily adapted for electric fields.

In the presence of a large-scale magnetic field \mathbf{B} , the amplitude of the photon γ scattering with \mathbf{B} and producing the axion a reads

$$\mathcal{A}_{\gamma \rightarrow a} \propto g_{a\gamma} \langle a | \sqrt{a} \sqrt{a} \mathbf{E} \cdot \mathbf{B} | \gamma \rangle, \quad (3.32)$$

where a and \mathbf{E} are quantized fields which are to be contracted with the initial and final single-particle states. In a consistent QFT treatment, \mathbf{B} should also be quantized, but due to the enormously large occupation number of quanta in the background, \mathbf{B} can be replaced by its classical field value.

Eq. (3.32) is interpreted as coherent scattering of the photon with the magnetic field. The scattering may happen at any point in the region with nonzero field strength, and all possible scattering amplitudes should be summed coherently, corresponding to an integration over the space. The outgoing axion may not have exactly the same momentum as the incoming photon, subjected to certain limitations from coherency. In particular, Eq. (3.32) also allows for coherent backward scattering, which means that the outgoing axion moves along the opposite direction as the incoming photon while still maintaining coherence. We leave discussions on these issues to Appendix A.

Assuming that the magnetic background is static and distributes vertically, one can prove (see also Appendix A) that the energy conservation and the conservation of momentum along the direction parallel to the magnetic field are respected, i.e.,

$$E_\gamma = E_a, \quad \mathbf{p}_{\gamma,\parallel} = \mathbf{p}_{a,\parallel}, \quad \mathbf{p}_{\gamma,\perp} \neq \mathbf{p}_{a,\perp}, \quad (3.33)$$

where the subscripts “ \perp ” and “ \parallel ” denote projections perpendicular and parallel to the magnetic field. For simplicity, below we assume $\mathbf{p}_{\gamma,\parallel} = \mathbf{p}_{a,\parallel} = 0$, i.e., \mathbf{p}_γ is perpendicular to \mathbf{B} .

In momentum space, the contraction in Eq. (3.32) leads to

$$\overline{\mathbf{E}}|\gamma\rangle \rightarrow \mathbf{p}_\gamma \overline{A^0}|\gamma\rangle + E_\gamma \overline{\mathbf{A}}|\gamma\rangle = \mathbf{p}_\gamma \epsilon^0 + E_\gamma \boldsymbol{\epsilon}, \quad \langle a|a \rangle \rightarrow 1, \quad (3.34)$$

where $(\epsilon^0, \boldsymbol{\epsilon})$ are the temporal and spatial components of the polarization vector ϵ^μ . Therefore, the amplitude is

$$\mathcal{A}_{\gamma \rightarrow a} \propto g_{a\gamma} E_\gamma \boldsymbol{\epsilon} \cdot \mathbf{B} = g_{a\gamma} E_\gamma B \cos \theta_\epsilon, \quad (3.35)$$

where θ_ϵ is defined as the angle between $\boldsymbol{\epsilon}$ and \mathbf{B} . The $\mathbf{p}_\gamma \epsilon^0$ term in Eq. (3.34) does not contribute because $\epsilon^0 = 0$ for massless photons. Eq. (3.35) implies that the photon-axion conversion rate becomes maximal when $\boldsymbol{\epsilon}$ is parallel to \mathbf{B} .

For the scalar interaction in Eq. (2.7), we have obtained a similar result:

$$\mathcal{A}_{\gamma \rightarrow \phi} \propto g_{\phi\gamma} (\mathbf{p}_\gamma \times \boldsymbol{\epsilon}) \cdot \mathbf{B} = g_{\phi\gamma} (\boldsymbol{\epsilon} \times \mathbf{B}) \cdot \mathbf{p}_\gamma = g_{\phi\gamma} E_\gamma B \sin \theta_\epsilon, \quad (3.36)$$

which implies that the conversion rate is maximal when $\boldsymbol{\epsilon}$ is perpendicular to \mathbf{B} .

Performing Fourier transform from momentum space to coordinate space (see Appendix A for details), we obtain the full expression of $\mathcal{A}_{\gamma \rightarrow a}$:

$$\mathcal{A}_{\gamma \rightarrow a} = \frac{g_{a\gamma} E_\gamma B \cos \theta_\epsilon}{2\sqrt{p_\gamma p_a}} \frac{e^{i|\mathbf{q}|L} - 1}{|\mathbf{q}|}, \quad (3.37)$$

where L denotes the length of the photon propagation in the \mathbf{B} field, $p_\gamma = E_\gamma$, $p_a = \sqrt{E_\gamma^2 - m_a^2}$, and $|\mathbf{q}| = E_\gamma - \sqrt{E_\gamma^2 - m_a^2}$. Squaring the amplitude, we obtain the transition probability:

$$P_{\gamma \rightarrow a} = \frac{g_{a\gamma}^2 B^2 \cos^2 \theta_\epsilon}{|\mathbf{q}|^2} \cdot \frac{E_\gamma}{p_a} \cdot \sin^2 \left(\frac{|\mathbf{q}|L}{2} \right). \quad (3.38)$$

For the inverse process $a \rightarrow \gamma$, the transition probability is the same—see discussions below Eq. (A.23).

Eq. (3.38) is to be compared with e.g. Eq. (25) in Ref. [7] (see also Eq. (16) in Ref. [9] and Eq. (16) in Ref. [52]). We note here that Eq. (3.38) remains valid even for non-relativistic axions, while previous results are only applicable to relativistic axions. The difference is accounted for by the E_γ/p_a factor.

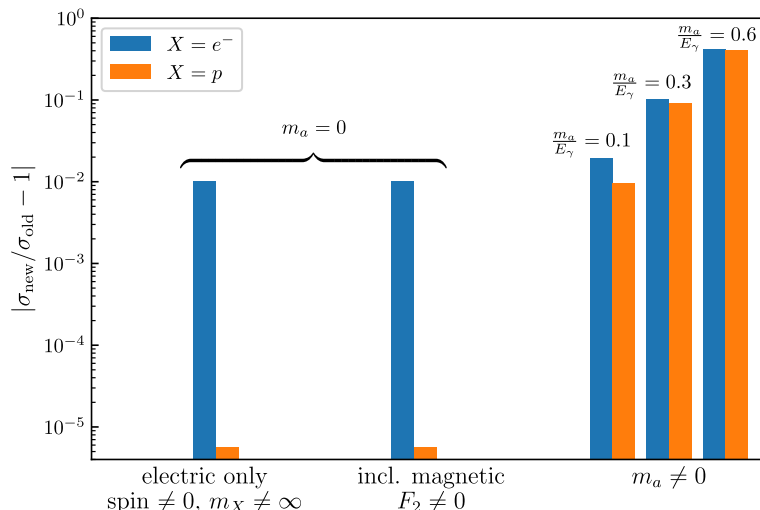


Figure 6. Deviations of the total cross section, denoted by σ_{new} , from the old one in Eq. (3.31) which is denoted by σ_{old} . The bar heights indicate the magnitudes of corrections due to various effects discussed in this work. In this figure, we take $E_\gamma = 3$ keV and $\kappa_s = 8$ keV.

3.7 Summary

In this section, we have comprehensively discussed various effects that can cause corrections to the Primakoff cross section. In previous studies, the most widely-adopted formula for the Primakoff cross section is Eq. (3.31), which is obtained assuming that (i) the axion is massless, and (ii) the target particle X is infinitely heavy ($m_X \rightarrow \infty$) such that its spin and magnetic moment can be neglected. Here we would like to discuss and compare the aforementioned corrections to this widely-adopted cross section.

For massless axions, the spin and magnetic moment corrections crucially depend on the finite mass m_X . This is shown in Fig. 6 by the four bars on the left. The first two bars labeled “electric only” with “spin $\neq 0$ ” and “ $m_X \neq \infty$ ” are obtained by integrating Eq. (3.5) over T_X , with Eq. (3.27) included, and comparing it with Eq. (3.31). The next two bars labeled “incl. magnetic” and “ $F_2 \neq 0$ ” show the corrections after further taking the F_2 factor into account. Since these effects would vanish in the limit of $m_X \rightarrow \infty$, the correction for $X = e^-$ is much more significant than that for $X = p$.

For massive axions, our new cross section can be significantly different from the old one, as is shown by the bars labeled “ $m_a \neq 0$ ” in Fig. 6. Here the correction due to the axion mass is much larger than the corrections caused by the spin and magnetic moment of the target particle. This correction has weak dependence on the target particle mass, making the correction for $X = p$ slightly lower than that for $X = e^-$.

From Fig. 6, we see that for massive axions with $m_a/E_\gamma \gtrsim 0.1$, the correction due to finite m_a is the dominant one. For $m_a/E_\gamma \ll 0.1$ and $X = e^-$, the spin and magnetic moment corrections become dominant, typically of the order of 1%. This $\sim 1\%$ correction cannot be reduced by $m_a \rightarrow 0$. Therefore, we conclude that the old formula in Eq. (3.31) is valid at $\sim 1\%$ precision in the massless limit. If higher precision is required or if the

finite- m_a correction is significant, the cross section should include the relevant corrections.

4 Solar axion flux

Given the crucial role the Sun has played in previous studies on axions and the actively ongoing experimental searches, we would like to apply our results in Sec. 3 to the calculation of solar axion flux⁵, aiming at providing an update of the previous result [9]:

$$\frac{d\Phi_a}{dE_a} = 6.02 \times 10^{10} \text{cm}^{-2} \text{s}^{-1} \text{keV}^{-1} g_{10}^2 \bar{E}_a^{2.481} e^{-\bar{E}_a/1.205}, \quad (4.1)$$

where $g_{10} \equiv g_{a\gamma} \times 10^{10}$ GeV and $\bar{E}_a \equiv E_a/\text{keV}$. Eq. (4.1) was first used by the CAST experiment [9] and also subsequently adopted by many solar axion searches at CDMS [10], EDELWEISS [11], MAJORANA [12]. It is obtained by integrating the Primakoff production rate for a solar model by Bahcall *et al* published in 2004 [54], assuming massless axions. The solar model dependence is recently examined by Ref. [55] and known to cause percent-level variations. We note here that the corrections to the cross section for massless axions can also be as large as 1%. Therefore, if percent-level accuracy of the solar axion flux is required, Eq. (4.1) needs to be revised by taking both the solar model dependence and the corrections to the cross section into account. For massive axions with $m_a/E_\gamma \gtrsim 0.1$, according to Fig. 6, the finite- m_a correction becomes more significant. Hence for keV axions, it is necessary to include the finite- m_a correction in the calculation of the solar axion flux.

In this work, we take an updated solar model and apply our more elaborated Primakoff cross section to recalculate the flux. In the massless limit, our flux is very close to Eq. (4.1) but for keV axions it deviates significantly from the vacuum limit. Therefore, our result would be important to solar axion search experiments using crystal [8, 10–12] or liquid xenon [16–19] detectors, which are sensitive to deposit energies above a few keV. Note that in this work we assume that the axion-electron coupling is absent, otherwise there is an additional contribution to the flux, the so-called ABC flux in the literature [56].

Let us first briefly review some basic formulae for the calculation of solar axion flux. The probability of a photon scattering off a medium particle (X) per unit time is $\sigma_X n_X$ where σ_X is the cross section of γ with X and n_X is number density of X . We sum over all possible medium particles so the total conversion rate of a photon into an axion reads:

$$\Gamma_{\gamma \rightarrow a} = \sum_X \sigma_X n_X. \quad (4.2)$$

If we take the simplified cross section in Eq. (3.31), $\Gamma_{\gamma \rightarrow a}$ can be written as

$$\Gamma_{\gamma \rightarrow a} = \frac{g_{a\gamma}^2 \kappa_s^2 T}{32\pi} \left[\left(1 + \frac{\kappa_s^2}{4E_\gamma^2} \right) \log \left(1 + \frac{4E_\gamma^2}{\kappa_s^2} \right) - 1 \right], \quad m_a \rightarrow 0 \ \& \ m_X \rightarrow \infty, \quad (4.3)$$

which agrees with Eq. (5) in Ref. [9]. For general values of m_a and m_X , we refer to Appendix B for the full expression of the cross section and use it in Eq. (4.2).

⁵For axions emitted from other stellar environments, we refer to Ref. [53]. In principle, given stellar interior profiles obtained from stellar simulations, our calculation presented in this work can be readily applied to other stars.

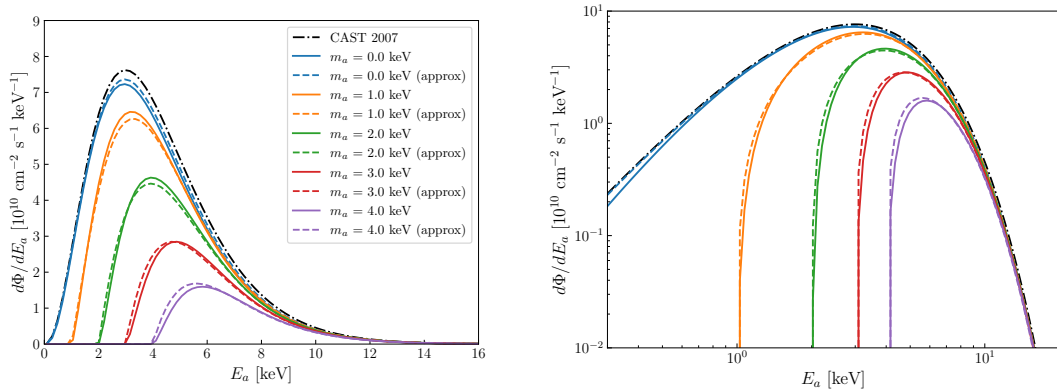


Figure 7. Solar axion flux computed in this work. The solid lines are obtained from our numerical calculation while the dashed lines are produced using the approximate expression in Eq. (4.5). The black dot-dashed line represents the CAST 2007 expression in Eq. (4.1). The right panel represents the left in log scales, with the same color code.

With $\Gamma_{\gamma \rightarrow a}$ obtained, the solar axion flux can be computed by

$$\frac{d\Phi_a}{dE_a} = \int_0^{R_\odot} dr \frac{r^2}{D_\odot^2} \cdot \frac{4\pi E_a^2}{(2\pi)^3} \cdot \frac{2}{e^{E_a/T} - 1} \Gamma_{\gamma \rightarrow a}, \quad (4.4)$$

where we have neglected the small difference between E_a and E_γ . The difference could be included by using the differential cross section multiplied by the photon distribution function, and integrating it with respect to E_γ .

Using Eqs. (4.2) and (4.4) with the cross section in Appendix B, we compute the solar axion flux for $m_a \in \{0, 1, 2, 3, 4\}$ keV and present the results in Fig. 7. For the solar model, we take B16-AGSS09met from Ref. [57].

As is shown in Fig. 7, our massless limit (blue curve) approximately agrees with the previous CAST 2007 result (black curve) given by Eq. (4.1). Our result is slightly lower than the previous, owing to solar model variations. The difference, however, becomes rather significant for the axion mass at the keV scale, implying that Eq. (4.1) should be modified when used for keV axion searches. In practice, we find that the following expression (shown as dashed lines in Fig. 7) can approximately fit our numerical result:

$$\frac{d\Phi_a}{dE_a} \approx 5.94 \times 10^{10} \text{cm}^{-2} \text{s}^{-1} \text{keV}^{-1} g_{10}^2 \bar{E}_a^{2.49} e^{-\bar{E}_a/1.19} S, \quad (4.5)$$


where S is an suppression factor to account for the mass correction:

$$S = \begin{cases} 1 - (m_a/E_a)^{1.67} & E_a > m_a \\ 0 & E_a \leq m_a \end{cases}. \quad (4.6)$$

Note that Eq. (4.5) should not be used in the strong Boltzmann suppression regime since the parametric fit is performed within an energy range up to ~ 10 keV. For higher axion masses or energies, the full numerical approach should be adopted to compute the

Boltzmann suppressed tail more accurately and, according to Ref. [58], the on-shell photon coalescence ($\gamma\gamma \rightarrow a$) should be included. This can be implemented by integrating $|\mathcal{M}_{\gamma\gamma \rightarrow a}|^2 = g_{a\gamma}^2 m_a^4/2$ with two photon distribution functions.

5 Conclusions

The Primakoff process has a pivotal role in the production and detection of axions in astrophysical environments and laboratories. Given the on-going activities in axion searches, we revisit this process and present a comprehensive calculation including various previously neglected factors. In this work, we adopt a consistent QFT derivation with rigorous treatment of the kinematics, and obtain Primakoff cross sections that are valid in the full mass range allowed by the kinematics. Regarding the photon-axion conversion in a magnetic background, we also obtain a new result that remains valid for non-relativistic axions. Further, we update the calculation of the solar axion flux, providing both a simple and practically useful expression [see Eq. (4.5)] and full numerical access with the code publicly available at GitHub . Compared to the previous widely-used one [see Eq. (4.1)], the most prominent difference in our new result is caused by the mass correction, which becomes significant for keV or heavier axions. Therefore, our work would be of particular importance to axion search experiments utilizing crystal and liquid xenon detectors.

Acknowledgments

We acknowledge the use of FEYNCALC [59–61] and PACKAGE-X⁶ [62, 63] in this work. X.-J. Xu is supported in part by the National Natural Science Foundation of China under grant No. 12141501 and also by the CAS Project for Young Scientists in Basic Research (YSBR-099). Q.-f. Wu is supported by the National Natural Science Foundation of China under grant No. 12075251.

A The QFT approach to coherent scattering with background fields

In this appendix, we show that the conversion between two particles such as the photon and the axion in a background field can be consistently derived in the QFT approach. Unlike the classical field approach which treats the incoming photon as an electromagnetic field and the outgoing axion as another oscillating field, the QFT approach treats incoming and outgoing states as single-particle states. The key concept here is that the incoming particle undergoes coherent scattering with the background field and is thereby converted to another particle, as we shall elucidate below.

We start by considering a toy model which contains two massive scalar field ϕ_1 and ϕ_2 , with different masses m_1 and m_2 , coupled to a background scalar field Φ as follows:

$$\mathcal{L} = \sum_{i=1,2} \left(\frac{1}{2} \partial^\mu \phi_i \partial_\mu \phi_i - \frac{1}{2} m_i^2 \phi_i^2 \right) + \phi_1 \phi_2 \Phi^2. \quad (\text{A.1})$$

⁶This package is available at <https://gitlab.com/mule-tools/package-x.git>.

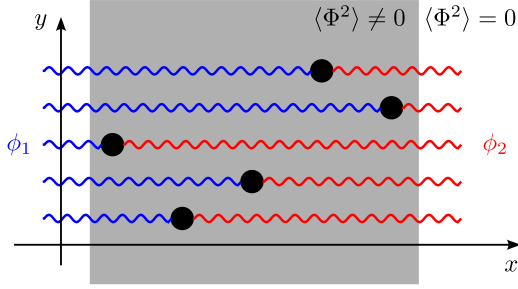


Figure 8. Conversion of a ϕ_1 particle (blue) to a ϕ_2 particle (red) in the background field Φ (gray region) via the interaction $\phi_1\phi_2\Phi^2$. The conversion may occur at any point in the gray region and the overall effect can be viewed as coherent scattering of ϕ_1 with the background field, with all possible scattering amplitudes added coherently.

The background field Φ has a nonzero expectation value only within a slice of space that extends infinitely along the y and z axis, but is bounded along the x axis:

$$\langle \Phi^2 \rangle = \begin{cases} v^2 & (a \leq x \leq b) \\ 0 & (\text{otherwise}) \end{cases}. \quad (\text{A.2})$$

Now consider a ϕ_1 particle moving along the x axis and going through this slice of space. Due to the interaction $\phi_1\phi_2\Phi^2$, there is a certain probability that the ϕ_1 particle may be converted to a ϕ_2 particle, as illustrated by Fig. 8.

Denote the momenta of the ϕ_1 and ϕ_2 particles by $p_1^\mu = (E_1, \mathbf{p}_1)$ and $p_2^\mu = (E_2, \mathbf{p}_2)$. Since the background field is static and $m_1 \neq m_2$, we expect that

$$E_1 = E_2, \quad (\text{A.3})$$

$$\mathbf{p}_1 \neq \mathbf{p}_2. \quad (\text{A.4})$$

Eqs. (A.3) and (A.4) will be derived later. Here let us first discuss the physical implication of Eqs. (A.3) and (A.4). The momentum difference $\mathbf{q} = \mathbf{p}_1 - \mathbf{p}_2$ can be interpreted as the momentum transferred from ϕ_1 to the background. For coherent scattering, the inverse of the momentum transfer needs to be much greater than the geometric dimension of the target. As we are only concerned with the x direction, this implies

$$|\mathbf{q}| \ll L^{-1}, \quad (\text{A.5})$$

where $|\mathbf{q}| = p_{1x} - \sqrt{p_{1x}^2 - \delta m^2}$ with $\delta m^2 \equiv m_2^2 - m_1^2$, and $L = b - a$ is the width of the gray region in Fig. 8. When Eq. (A.5) is satisfied, full coherency is achieved, implying that the scattering amplitude is proportional to L , hence the conversion probability proportional to L^2 :

$$P_{\phi_1 \rightarrow \phi_2} \propto L^2. \quad (\text{A.6})$$

As we will see, indeed the result derived later exhibits this feature when Eq. (A.5) is satisfied.

Below we present the calculation.

The amplitude of the ϕ_1 particle being converted to ϕ_2 reads:

$$i\mathcal{A} \equiv \langle 2 | e^{i \int H_I dt} | 1 \rangle, \quad (\text{A.7})$$

where H_I is the interaction Hamiltonian and the initial and final states are defined as

$$|i\rangle \equiv \int \frac{d\mathbf{k}_i}{(2\pi)^3} \frac{1}{\sqrt{2E_{\mathbf{k}_i}}} w_i(\mathbf{k}_i) |\mathbf{k}_i\rangle, \quad |\mathbf{k}_i\rangle = \sqrt{2E_{\mathbf{k}_i}} a_{\mathbf{k}_i}^\dagger |0\rangle, \quad i = 1, 2. \quad (\text{A.8})$$

Note that $|\mathbf{k}_i\rangle$ is a single-particle state normalized in the QFT convention, $\langle \mathbf{k}'_i | \mathbf{k}_i \rangle = 2E_{\mathbf{k}_i} (2\pi)^3 \delta^3(\mathbf{k}_i - \mathbf{k}'_i)$ which is Lorentz invariant, while $|i\rangle$ wraps $|\mathbf{k}_i\rangle$ with a normalized wavefunction $w_i(\mathbf{k}_i)$ such that

$$\langle i | i \rangle = 1 \quad \Leftrightarrow \quad \int \frac{d\mathbf{k}_i}{(2\pi)^3} |w_i(\mathbf{k}_i)|^2 = 1. \quad (\text{A.9})$$

The momentum distribution of $w_i(\mathbf{k}_i)$ is assumed to be centered around \mathbf{p}_i with a very small but nonvanishing width such that at macroscopic scales the two particles can be localized in both momentum space and coordinate space—for further explanation, see Appendix A of Ref. [64]. The specific form of $w_i(\mathbf{k}_i)$ is unimportant as long as it satisfies the aforementioned requirements.

The interaction Hamiltonian $H_I = \int \phi_1 \phi_2 \Phi^2 d^3\mathbf{x}$ is assumed to be perturbative, which implies $i\mathcal{A} \approx \langle 2 | i \int H_I dt | 1 \rangle \approx i \int \langle 2 | \phi_1 \phi_2 \Phi^2 | 1 \rangle d^4x$.

To proceed, we need to calculate

$$\mathcal{C} \equiv \overbrace{\langle \mathbf{k}_2 | \phi_1(x) \phi_2(x) \Phi^2(x) | \mathbf{k}_1 \rangle}. \quad (\text{A.10})$$

The quantized fields ϕ_1 and ϕ_2 (for simplicity, we omit the subscripts when they are unimportant) are given by

$$\phi(x) = \int \frac{d\mathbf{k}}{(2\pi)^3} \frac{1}{\sqrt{2E_{\mathbf{k}}}} \left(a_{\mathbf{k}} e^{-ik \cdot x} + a_{\mathbf{k}}^\dagger e^{ik \cdot x} \right). \quad (\text{A.11})$$

From Eq. (A.11) and the definition of $|\mathbf{k}\rangle$ in Eq. (A.8), we obtain

$$\overbrace{\phi(x) | \mathbf{k} \rangle} = e^{-ik \cdot x} |0\rangle. \quad (\text{A.12})$$

Hence, Eq. (A.10) becomes

$$\mathcal{C}(x) = e^{ik_2 \cdot x} e^{-ik_1 \cdot x} \Phi^2(x). \quad (\text{A.13})$$

Thus, the scattering amplitude is

$$i\mathcal{A} = i \int d^4x \Phi^2(x) \int \frac{d^3\mathbf{k}_1}{(2\pi)^3} \frac{d\mathbf{k}_2}{(2\pi)^3} \frac{e^{i(k_2 - k_1) \cdot x}}{\sqrt{2E_{\mathbf{k}_1} 2E_{\mathbf{k}_2}}} w_1(\mathbf{k}_1) w_2^*(\mathbf{k}_2). \quad (\text{A.14})$$

Since the background field $\Phi(x)$ is time independent, we can integrate out dt with the time-dependent part of $e^{i(k_2 - k_1) \cdot x}$, giving rise to a Dirac delta function. Similar integration

for the spatial coordinates y and z can also be performed. Overall, we obtain three Dirac delta functions:

$$\int d^4x \Phi^2(x) e^{i(k_2 - k_1) \cdot x} = (2\pi)^3 \delta(E_{\mathbf{k}_1} - E_{\mathbf{k}_2}) \delta(k_{1y} - k_{2y}) \delta(k_{1z} - k_{2z}) \times \tilde{\Phi}^2(k_{2x} - k_{1x}), \quad (\text{A.15})$$

where $\tilde{\Phi}^2$ denotes the Fourier transform of Φ^2 :

$$\tilde{\Phi}^2(k) \equiv \int dx \Phi^2(x) e^{-ikx}. \quad (\text{A.16})$$

Eq. (A.15) implies that the incoming and outgoing particles should have the same energy as well as the same momentum in the y - z plane. Since they have different masses, their momenta along the x axis have to be different.

Substituting Eq. (A.15) into Eq. (A.14), it is straightforward to integrate out k_{2y} and k_{2z} with two of the delta functions, while the remaining one is to be integrated out by k_{2x} :

$$\int dk_{2x} \delta(E_{\mathbf{k}_1} - E_{\mathbf{k}_2}) \rightarrow \frac{E_{\mathbf{k}_1}}{\sqrt{E_{\mathbf{k}_1}^2 - \tilde{m}_2^2}} = \frac{E_{\mathbf{k}_1}}{k_{2x}}, \quad (\text{A.17})$$

where $\tilde{m}_2^2 \equiv m_2^2 + k_{2y}^2 + k_{2z}^2$.

Note that when integrating k_{2x} from $-\infty$ to ∞ in Eq. (A.17), there are two poles in $\delta(E_{\mathbf{k}_1} - E_{\mathbf{k}_2})$, one at $k_{2x} = \sqrt{E_{\mathbf{k}_1}^2 - \tilde{m}_2^2}$ and the other at $k_{2x} = -\sqrt{E_{\mathbf{k}_1}^2 - \tilde{m}_2^2}$. Both are physical solutions and can be understood intuitively, one corresponding to coherent forward scattering and the other to coherent backward scattering. We drop the latter since our derivation is focused on coherent forward scattering.

After integrating out all the three delta functions, we obtain

$$\begin{aligned} i\mathcal{A} &= i \int \frac{d^3\mathbf{k}_1}{(2\pi)^3} \tilde{\Phi}^2(k_{2x} - k_{1x}) \frac{1}{\sqrt{2E_{\mathbf{k}_1} 2E_{\mathbf{k}_2}}} \frac{E_{\mathbf{k}_1}}{k_{2x}} w_1(\mathbf{k}_1) w_2^*(\mathbf{k}_2) \Big|_{\mathbf{k}_2 \rightarrow (k_{2x}, k_{1y}, k_{1z})} \\ &= i \int \frac{d^3\mathbf{k}_1}{(2\pi)^3} \frac{\tilde{\Phi}^2(k_{2x} - k_{1x})}{2k_{2x}} w_1(\mathbf{k}_1) w_2^*(\mathbf{k}_2) \Big|_{\mathbf{k}_2 \rightarrow (k_{2x}, k_{1y}, k_{1z})} \\ &= i \frac{\tilde{\Phi}^2(-|\mathbf{q}|)}{2p_{2x}} \left(\frac{p_{2x}}{p_{1x}} \right)^{1/2} \\ &= i \frac{\tilde{\Phi}^2(-|\mathbf{q}|)}{2\sqrt{p_{2x} p_{1x}}}, \end{aligned} \quad (\text{A.18})$$

where in the third step we have squeezed w_1 and w_2 to their delta function limits [see the comments below Eq. (A.9)]:

$$w_1(\mathbf{k}_1) w_2^*(\mathbf{k}_2) \rightarrow (2\pi)^3 \sqrt{\delta^3(\mathbf{k}_1 - \mathbf{p}_1)} \sqrt{\delta^3(\mathbf{k}_2 - \mathbf{p}_2)}. \quad (\text{A.19})$$

Since the y and z components of \mathbf{p}_1 (\mathbf{k}_1) and \mathbf{p}_2 (\mathbf{k}_2) are identical, we have $\delta(k_{2y} - p_{2y}) = \delta(k_{1y} - p_{1y})$ and $\delta(k_{2z} - p_{2z}) = \delta(k_{1z} - p_{1z})$. The part along the x axis however requires an additional treatment:

$$\delta(k_{2x} - p_{2x}) \rightarrow \delta(k_{1x} - p_{1x}) \left| \frac{\partial k_{2x}}{\partial k_{1x}} \right|^{-1} = \delta(k_{1x} - p_{1x}) \frac{p_{2x}}{p_{1x}}. \quad (\text{A.20})$$

So for the toy model, our final result of the coherent forward scattering amplitude is

$$\mathcal{A} = \frac{1}{2\sqrt{p_{2x}p_{1x}}} \int dx \Phi^2(x) e^{i|\mathbf{q}|x} \quad (\text{A.21})$$

$$= \frac{v^2}{2\sqrt{p_{2x}p_{1x}}} \cdot \frac{e^{i|\mathbf{q}|b} - e^{i|\mathbf{q}|a}}{|\mathbf{q}|}, \quad (\text{A.22})$$

where in the second step we have used the profile of $\Phi^2(x)$ in Eq. (A.2). Note that Eq. (A.21) can be generally applied to arbitrary profiles of $\Phi^2(x)$, provided that it only varies along the x -axis direction.

The conversion probability is thus given by

$$P_{\phi_1 \rightarrow \phi_2} = |\mathcal{A}|^2 = \frac{v^4}{p_{2x}p_{1x}|\mathbf{q}|^2} \sin^2\left(\frac{|\mathbf{q}|L}{2}\right). \quad (\text{A.23})$$

This verifies our previous argument about coherency that the probability is proportional to L^2 when $|\mathbf{q}|$ is small—see Eq. (A.6). Eq. (A.23) is symmetric under the exchange of $1 \leftrightarrow 2$, which implies that the inverse process has the same conversion probability, $P_{\phi_2 \rightarrow \phi_1} = P_{\phi_1 \rightarrow \phi_2}$.

The above calculation can be straightforwardly adapted to other scenarios involving particles with internal degrees of freedom such as spins or polarizations. For the photon-axion conversion in a magnetic field, after proper treatments of the polarization of the photon and the orientation of the magnetic field, as has been addressed in Sec. 3.6, the derivation is very similar if we replace $v^2 \rightarrow g_{a\gamma} \langle B \rangle E_\gamma$.

B Full expression of the total cross section including Debye-Hückel screening

The total cross section of $\gamma + X \rightarrow a + X$, after including Debye-Hückel screening into Eq. (3.5) and integrating out T_X , is given as follows:

$$\begin{aligned} \sigma_{\text{tot}} = & \frac{\alpha g_{a\gamma}^2 Q_X^2}{128 E_\gamma^2 m_X^2} [(q_+^2 - q_-^2) (4m_a^2 - 8E_\gamma m_X - 4m_X^2 + q_-^2 + q_+^2 - 2\kappa_s^2) \\ & + 2L_2 (8E_\gamma^2 m_X^2 + m_a^4 - 4E_\gamma m_a^2 m_X - 4m_a^2 m_X^2) \\ & + 2L_2 (2\kappa_s^2 (2E_\gamma m_X + m_X^2 - m_a^2) + 2m_a^4 m_X^2 / \kappa_s^2 + \kappa_s^4) \\ & - 4L_1 m_a^4 m_X^2 / \kappa_s^2], \end{aligned} \quad (\text{B.1})$$

where

$$q_\pm^2 \equiv \frac{2E_\gamma^2 m_X - m_a^2 (E_\gamma + m_X) \pm E_\gamma \sqrt{4E_\gamma^2 m_X^2 - 4m_a^2 m_X (E_\gamma + m_X) + m_a^4}}{2E_\gamma + m_X}, \quad (\text{B.2})$$

$$L_1 \equiv \log\left(\frac{q_+^2}{q_-^2}\right), \quad L_2 \equiv \log\left(\frac{q_+^2 + \kappa_s^2}{q_-^2 + \kappa_s^2}\right). \quad (\text{B.3})$$

References

- [1] H. Primakoff, *Photoproduction of neutral mesons in nuclear electric fields and the mean life of the neutral meson*, *Phys. Rev.* **81** (1951) 899.
- [2] R.D. Peccei and H.R. Quinn, *CP conservation in the presence of pseudoparticles*, *Phys. Rev. Lett.* **38** (1977) 1440.
- [3] R.D. Peccei and H.R. Quinn, *Constraints imposed by CP conservation in the presence of pseudoparticles*, *Phys. Rev. D* **16** (1977) 1791.
- [4] S. Weinberg, *A new light boson?*, *Phys. Rev. Lett.* **40** (1978) 223.
- [5] F. Wilczek, *Problem of strong p and t invariance in the presence of instantons*, *Phys. Rev. Lett.* **40** (1978) 279.
- [6] G.G. Raffelt, *Stars as laboratories for fundamental physics: The astrophysics of neutrinos, axions, and other weakly interacting particles*, University of Chicago Press (1996).
- [7] A. Caputo and G. Raffelt, *Astrophysical axion bounds: The 2024 edition*, in *1st Training School of the COST Action COSMIC WISPerS (CA21106)*, 1, 2024 [[2401.13728](#)].
- [8] SOLAX collaboration, *Experimental search for solar axions via coherent primakoff conversion in a germanium spectrometer*, *Phys. Rev. Lett.* **81** (1998) 5068 [[astro-ph/9708008](#)].
- [9] CAST collaboration, *An improved limit on the axion-photon coupling from the cast experiment*, *JCAP* **04** (2007) 010 [[hep-ex/0702006](#)].
- [10] CDMS collaboration, *Search for axions with the cdms experiment*, *Phys. Rev. Lett.* **103** (2009) 141802 [[0902.4693](#)].
- [11] E. Armengaud et al., *Axion searches with the edelweiss-ii experiment*, *JCAP* **11** (2013) 067 [[1307.1488](#)].
- [12] MAJORANA collaboration, *Search for solar axions via axion-photon coupling with the majorana demonstrator*, *Phys. Rev. Lett.* **129** (2022) 081803 [[2206.05789](#)].
- [13] G.G. Raffelt, *Astrophysical axion bounds diminished by screening effects*, *Phys. Rev. D* **33** (1986) 897.
- [14] D.A. Dicus, E.W. Kolb, V.L. Teplitz and R.V. Wagoner, *Astrophysical bounds on the masses of axions and higgs particles*, *Phys. Rev. D* **18** (1978) 1829.
- [15] CAST collaboration, *New cast limit on the axion-photon interaction*, *Nature Phys.* **13** (2017) 584 [[1705.02290](#)].
- [16] K. Abe et al., *Search for solar axions in xmass, a large liquid-xenon detector*, *Phys. Lett. B* **724** (2013) 46 [[1212.6153](#)].
- [17] XENON100 collaboration, *First axion results from the xenon100 experiment*, *Phys. Rev. D* **90** (2014) 062009 [[1404.1455](#)].
- [18] C. Gao, J. Liu, L.-T. Wang, X.-P. Wang, W. Xue and Y.-M. Zhong, *Reexamining the Solar Axion Explanation for the XENON1T Excess*, *Phys. Rev. Lett.* **125** (2020) 131806 [[2006.14598](#)].
- [19] J.B. Dent, B. Dutta, J.L. Newstead and A. Thompson, *Inverse Primakoff Scattering as a Probe of Solar Axions at Liquid Xenon Direct Detection Experiments*, *Phys. Rev. Lett.* **125** (2020) 131805 [[2006.15118](#)].

- [20] T. Dafni, C.A.J. O’Hare, B. Lakić, J. Galán, F.J. Iguaz, I.G. Irastorza et al., *Weighing the solar axion*, *Phys. Rev. D* **99** (2019) 035037 [[1811.09290](#)].
- [21] J. Jaeckel and L.J. Thormaehlen, *Axions as a probe of solar metals*, *Phys. Rev. D* **100** (2019) 123020 [[1908.10878](#)].
- [22] A. Banerjee, D. Budker, J. Eby, V.V. Flambaum, H. Kim, O. Matsedonskyi et al., *Searching for Earth/Solar Axion Halos*, *JHEP* **09** (2020) 004 [[1912.04295](#)].
- [23] A. Bhusal, N. Houston and T. Li, *Searching for Solar Axions Using Data from the Sudbury Neutrino Observatory*, *Phys. Rev. Lett.* **126** (2021) 091601 [[2004.02733](#)].
- [24] L. Di Luzio, M. Fedele, M. Giannotti, F. Mescia and E. Nardi, *Solar axions cannot explain the XENON1T excess*, *Phys. Rev. Lett.* **125** (2020) 131804 [[2006.12487](#)].
- [25] C. Cai, H.H. Zhang, M.T. Frandsen, M. Rosenlyst and G. Cacciapaglia, *XENON1T solar axion and the Higgs boson emerging from the dark*, *Phys. Rev. D* **102** (2020) 075018 [[2006.16267](#)].
- [26] C.A.J. O’Hare, A. Caputo, A.J. Millar and E. Vitagliano, *Axion helioscopes as solar magnetometers*, *Phys. Rev. D* **102** (2020) 043019 [[2006.10415](#)].
- [27] E. Guarini, P. Carena, J. Galan, M. Giannotti and A. Mirizzi, *Production of axionlike particles from photon conversions in large-scale solar magnetic fields*, *Phys. Rev. D* **102** (2020) 123024 [[2010.06601](#)].
- [28] M. Bastero-Gil, C. Beaufort and D. Santos, *Solar axions in large extra dimensions*, *JCAP* **10** (2021) 048 [[2107.13337](#)].
- [29] W. DeRocco, S. Wegsman, B. Grefenstette, J. Huang and K. Van Tilburg, *First Indirect Detection Constraints on Axions in the Solar Basin*, *Phys. Rev. Lett.* **129** (2022) 101101 [[2205.05700](#)].
- [30] G. Lucente, N. Nath, F. Capozzi, M. Giannotti and A. Mirizzi, *Probing high-energy solar axion flux with a large scintillation neutrino detector*, *Phys. Rev. D* **106** (2022) 123007 [[2209.11780](#)].
- [31] C. Beaufort, M. Bastero-Gil, T. Luce and D. Santos, *New solar x-ray constraints on keV axionlike particles*, *Phys. Rev. D* **108** (2023) L081302 [[2303.06968](#)].
- [32] S. Hoof, J. Jaeckel and L.J. Thormaehlen, *Axion helioscopes as solar thermometers*, *JCAP* **10** (2023) 024 [[2306.00077](#)].
- [33] D. Aloni, C. Fanelli, Y. Soreq and M. Williams, *Photoproduction of axionlike particles*, *Phys. Rev. Lett.* **123** (2019) 071801 [[1903.03586](#)].
- [34] M.S. Pshirkov and S.B. Popov, *Conversion of dark matter axions to photons in magnetospheres of neutron stars*, *J. Exp. Theor. Phys.* **108** (2009) 384 [[0711.1264](#)].
- [35] F.P. Huang, K. Kadota, T. Sekiguchi and H. Tashiro, *Radio telescope search for the resonant conversion of cold dark matter axions from the magnetized astrophysical sources*, *Phys. Rev. D* **97** (2018) 123001 [[1803.08230](#)].
- [36] A. Hook, Y. Kahn, B.R. Safdi and Z. Sun, *Radio signals from axion dark matter conversion in neutron star magnetospheres*, *Phys. Rev. Lett.* **121** (2018) 241102 [[1804.03145](#)].
- [37] B.R. Safdi, Z. Sun and A.Y. Chen, *Detecting axion dark matter with radio lines from neutron star populations*, *Phys. Rev. D* **99** (2019) 123021 [[1811.01020](#)].

- [38] R.A. Battye, B. Garbrecht, J.I. McDonald, F. Pace and S. Srinivasan, *Dark matter axion detection in the radio/mm-waveband*, *Phys. Rev. D* **102** (2020) 023504 [[1910.11907](#)].
- [39] M. Leroy, M. Chianese, T.D.P. Edwards and C. Weniger, *Radio signal of axion-photon conversion in neutron stars: A ray tracing analysis*, *Phys. Rev. D* **101** (2020) 123003 [[1912.08815](#)].
- [40] J.W. Foster, Y. Kahn, O. Macias, Z. Sun, R.P. Eatough, V.I. Kondratiev et al., *Green bank and effelsberg radio telescope searches for axion dark matter conversion in neutron star magnetospheres*, *Phys. Rev. Lett.* **125** (2020) 171301 [[2004.00011](#)].
- [41] A. Prabhu, *Axion production in pulsar magnetosphere gaps*, *Phys. Rev. D* **104** (2021) 055038 [[2104.14569](#)].
- [42] S.J. Witte, D. Noordhuis, T.D.P. Edwards and C. Weniger, *Axion-photon conversion in neutron star magnetospheres: The role of the plasma in the goldreich-julian model*, *Phys. Rev. D* **104** (2021) 103030 [[2104.07670](#)].
- [43] R.A. Battye, J. Darling, J.I. McDonald and S. Srinivasan, *Towards robust constraints on axion dark matter using psr j1745-2900*, *Phys. Rev. D* **105** (2022) L021305 [[2107.01225](#)].
- [44] A.J. Millar, S. Baum, M. Lawson and M.C.D. Marsh, *Axion-photon conversion in strongly magnetised plasmas*, *JCAP* **11** (2021) 013 [[2107.07399](#)].
- [45] J.W. Foster, S.J. Witte, M. Lawson, T. Linden, V. Gajjar, C. Weniger et al., *Extraterrestrial axion search with the breakthrough listen galactic center survey*, *Phys. Rev. Lett.* **129** (2022) 251102 [[2202.08274](#)].
- [46] D. Noordhuis, A. Prabhu, S.J. Witte, A.Y. Chen, F. Cruz and C. Weniger, *Novel constraints on axions produced in pulsar polar-cap cascades*, *Phys. Rev. Lett.* **131** (2023) 111004 [[2209.09917](#)].
- [47] R.A. Battye, M.J. Keith, J.I. McDonald, S. Srinivasan, B.W. Stappers and P. Weltevrede, *Searching for time-dependent axion dark matter signals in pulsars*, *Phys. Rev. D* **108** (2023) 063001 [[2303.11792](#)].
- [48] D. Noordhuis, A. Prabhu, C. Weniger and S.J. Witte, *Axion clouds around neutron stars*, [2307.11811](#).
- [49] A. Caputo, S.J. Witte, A.A. Philippov and T. Jacobson, *Pulsar nulling and vacuum radio emission from axion clouds*, [2311.14795](#).
- [50] PARTICLE DATA GROUP collaboration, *Review of Particle Physics*, *PTEP* **2020** (2020) 083C01.
- [51] G.G. Raffelt, *Astrophysical axion bounds*, *Lect. Notes Phys.* **741** (2008) 51 [[hep-ph/0611350](#)].
- [52] K. van Bibber, P.M. McIntyre, D.E. Morris and G.G. Raffelt, *Design for a practical laboratory detector for solar axions*, *Phys. Rev. D* **39** (1989) 2089.
- [53] N.H. Nguyen, E.H. Tanin and M. Kamionkowski, *Spectra of axions emitted from main sequence stars*, *JCAP* **11** (2023) 091 [[2307.11216](#)].
- [54] J.N. Bahcall and M.H. Pinsonneault, *What do we (not) know theoretically about solar neutrino fluxes?*, *Phys. Rev. Lett.* **92** (2004) 121301 [[astro-ph/0402114](#)].
- [55] S. Hoof, J. Jaeckel and L.J. Thormaehlen, *Quantifying uncertainties in the solar axion flux and their impact on determining axion model parameters*, *JCAP* **09** (2021) 006 [[2101.08789](#)].

- [56] J. Redondo, *Solar axion flux from the axion-electron coupling*, *JCAP* **12** (2013) 008 [[1310.0823](#)].
- [57] N. Vinyoles, A.M. Serenelli, F.L. Villante, S. Basu, J. Bergström, M.C. Gonzalez-Garcia et al., *A new generation of standard solar models*, *Astrophys. J.* **835** (2017) 202 [[1611.09867](#)].
- [58] G. Lucente, O. Straniero, P. Carenza, M. Giannotti and A. Mirizzi, *Constraining heavy axionlike particles by energy deposition in globular cluster stars*, *Phys. Rev. Lett.* **129** (2022) 011101 [[2203.01336](#)].
- [59] R. Mertig, M. Bohm and A. Denner, *FEYN CALC: Computer algebraic calculation of Feynman amplitudes*, *Comput. Phys. Commun.* **64** (1991) 345.
- [60] V. Shtabovenko, R. Mertig and F. Orellana, *New Developments in FeynCalc 9.0*, *Comput. Phys. Commun.* **207** (2016) 432 [[1601.01167](#)].
- [61] V. Shtabovenko, R. Mertig and F. Orellana, *FeynCalc 9.3: New features and improvements*, *Comput. Phys. Commun.* **256** (2020) 107478 [[2001.04407](#)].
- [62] H.H. Patel, *Package-X: A Mathematica package for the analytic calculation of one-loop integrals*, *Comput. Phys. Commun.* **197** (2015) 276 [[1503.01469](#)].
- [63] H.H. Patel, *Package-X 2.0: A Mathematica package for the analytic calculation of one-loop integrals*, *Comput. Phys. Commun.* **218** (2017) 66 [[1612.00009](#)].
- [64] A.Y. Smirnov and X.-J. Xu, *Neutrino bound states and bound systems*, *JHEP* **08** (2022) 170 [[2201.00939](#)].